



# Green synthesis of ZnO NPs using *Pontederia crassipes* leaf extract: characterization, their adsorption behavior and anti-cancer property

Mahmood A. Albo Hay Allah<sup>1,2</sup> · Hassan A. Alshamsi<sup>1</sup>

Received: 12 May 2022 / Revised: 11 July 2022 / Accepted: 13 July 2022 / Published online: 28 July 2022  
© The Author(s), under exclusive licence to Springer-Verlag GmbH Germany, part of Springer Nature 2022

## Abstract

The fabrication of nanoparticles by green routes is gaining extensive attention owing to their reliability, sustainability, being eco-friendly, cost-effectiveness, high productivity, and purity and biocompatibility. In the current study, zinc oxide nanoparticles (ZnO NPs) were successfully fabricated via green route using leaf extract of *Pontederia crassipes*. The synthesized sample was characterized by various techniques, such as FT-IR, XRD, BET, FEEM, TEM, and EDS. The characterization results confirmed the success of the synthesis process, with prepared ZnO NPs exhibiting good purity. The synthesized ZnO NPs were employed as an adsorbent for the removal of carcinogenic anionic congo red (CR) and cationic malachite green (MG) dyes from aqueous solutions. All experiments were performed in a batch process where the effects of dye concentration, adsorbent dose, equilibrium time, temperature, pH, and salinity have been investigated. High removal capacity of 96.39% for CR was achieved with pH 2, dye concentration of 40 mg/L, and adsorbent dosage of 1.2 g within 30-min equilibration time. On the other hand, the maximum adsorption efficiency for MG dye was 95.75% with pH 7, dye concentration of 15 mg/L, and ZnO dosage of 1.2 g within 60-min equilibration time. The Temkin and Freundlich isotherm models match the dye adsorption process for CR and MG, respectively. Depending on the thermodynamic functions, it was proven that the adsorption process for both dyes is endothermic and spontaneous. Employing ZnO as anti-breast cancer (MCF7 cancer cell line) was also studied. ZnO NPs exhibit high in vitro cytotoxic efficacy against cancerous MCF7 ( $IC_{50} = 39.3 \mu\text{g/mL}$ ).

**Keywords** Green synthesis · *Pontederia crassipes* · Adsorption · ZnO NPs · CR · MG · MCF7 cancer cell line · Anti-cancer

## 1 Introduction

Industrialization and population expansion have been steadily increasing over the last several decades, resulting in the release of a range of new contaminants into the aquatic environment [1]. Among the most hazardous materials that are released into aquatic environment are the highly soluble colorants. The risk of most synthetic colorants arises from the fact that they resist natural biodegradation due to their rigid chemical structure. Hazardous dye effluents emitted from sectors including textiles, papers, leather, and printing can have serious environmental and human health consequences [2]. Examples of commonly used organic dyes

are congo red (CR) and malachite green (MG) dyes. MG is a triphenylmethane-based cationic dye. Its chromophore groups are protonated in low-pH water with a pKa of 10.3 [3]. MG is extensively used in coloring cotton, jute, paper, silk, wool, and leather. Despite its diverse applications and due to its poisonous properties, the existence of MG in water has harmful impacts on aquatic life and human health, MG causes damage to the liver, spleen, kidneys, and heart. On the other hand, CR dye is an anionic dye with a pKa of 4.5 [4]. It is widely used in paper, rubber, textile, and plastic industries [5]. In water, it turns into a red colloidal solution, in which it is expected to metabolize to benzidine, a substance that has been proven to be mutagenic and carcinogenic to aquatic organisms [6]. In parallel to the exacerbation of the pollution problem, both qualitatively and quantitatively, scientists and researchers have faced huge challenges to find out efficient ways to get rid of or reduce the risks of these pollutants. Several effective pollution treatment methods have been developed, including physical, chemical, and biological processes. Regarding pollutant organic dyes, the heterogeneous

✉ Hassan A. Alshamsi  
Hassan.Habeeb@qu.edu.iq

<sup>1</sup> Department of Chemistry, College of Education, University of Al-Qadisiyah, Al-Diwaniyah, Iraq

<sup>2</sup> Ministry of Education, Educational Directorate of Karbala, Karbala, Iraq

photocatalysis and adsorption processes are the most important and efficient treatment processes. Comparatively, the adsorption technique is a trendy treatment way to remove various types of water contaminations, even at low concentrations, due to its abundancy, efficiency, and safety. Among the most important adsorbents used efficiently to remove various water contaminations is zinc oxide nanoparticles (ZnO NPs) [7]. Methods such as sol–gel [8], chemical precipitation [9], and hydrothermal [10] have been used extensively to fabricate mesoporous ZnO NPs. The employment of the aforementioned methods is associated with some disadvantages like using harmful chemicals, needing high-cost equipments, and consuming high energy. Recently, new alternative eco-friendly methods have been developed, such as the green approach, which have witnessed great interest, and at the same time, a relative decline of the classical methods in the various research fields has increased. According to a large number of previous reports, sustainable and green synthesis using plant extracts and other natural sources has reduced the adverse effects that are commonly associated with chemical synthesis. Nowadays, nanotechnologies are supplying a long range of new synthetic routes that improve the quality of the material adopting novel eco-friendly and biological synthetic ways [11–15]. ZnO has been used in many environmental, biological, and medical applications as a result of its safe and biologically compatible properties [16]. ZnO can be utilized as an anti-cancer [17], antimicrobial [18], and anti-fungal agent [19] due to its remarkable physicochemical assets. ZnO is considered a safe compound with the properties of photocatalysis and photo-oxidizing impacts on chemical and biological species of water contaminations [20, 21]. By looking at the results of a huge number of previously published reports, it has been proven that it can be utilized efficiently in many applications, particularly in the field of wastewater treatments [22–24]. *Pontederia crassipes* (water hyacinth) is an aquatic plant native to the Amazon basin and can be in many countries, especially those with hot climate. *Pontederia crassipes* has become a worldwide problem due to its rapid growth on surface waters in lakes, swamps, and narrow rivers [25]. Most plants, including *Pontederia crassipes*, possess different inherent phytochemicals, leading to the varying quality of green synthesized NPs. The leaves of *Pontederia crassipes* are rich with biologically active phytochemicals which can be utilized as reducing, stabilizing, and capping agents in the green approach. The current study aims to investigate the green synthesis of ZnO NPs adopting *Pontederia crassipes* leaf extract. Characterizing the fabricated NPs using FT-IR, XRD, FE-SEM, EDS, TEM, and BET analyses is another objective. Additionally, the behavior of ZnO NPs towards adsorptive removal of congo red and malachite green dyes from an aqueous solution was studied. The adsorption isotherms, kinetics, and thermodynamics of CO and MG over

ZnO NPs are also investigated. In addition, the synthesized ZnO NPs were employed and their anti-cancer (MCF7) properties were investigated.

## 2 Materials and methods

### 2.1 Chemicals

Zinc nitrate hexahydrate ( $\text{Zn}(\text{NO}_3)_2 \cdot 6\text{H}_2\text{O}$ , 99%), malachite green dye ( $\text{C}_{52}\text{H}_{54}\text{N}_4\text{O}_{12}$ , M.Wt. = 927 g/mol), congo red dye ( $\text{C}_{32}\text{H}_{22}\text{N}_6\text{Na}_2\text{O}_6\text{S}_2$  M.wt. = 696.7 g/mol), potassium chloride (KCl, 99%), and aluminum chloride ( $\text{AlCl}_3$ , 99%) were supplied by Merck. Sodium hydroxide (NaOH, 99%), hydrochloric acid (HCl, 37%), sodium chloride (NaCl, 99%), and calcium chloride ( $\text{CaCl}_2$ , 99%) were purchased from Scharlau.

#### 2.1.1 Preparation of *Pontederia crassipes* extract

Fresh leaves of *Pontederia crassipes* were collected from swamps near Al-Diwaniyah city (southern Iraq). The collected leaves were entirely rinsed several times using distilled water to remove adherent impurities, and then they were cut into small pieces. A weight of 10 g of the chopped leaves was added to 100 ml of deionized water, where the solution is constantly stirred using a magnetic stirrer at a speed of 180 rpm for 30 min at 80 °C. Afterwards, the mixture was filtered and the supernatant was stored in a refrigerator at a 4 °C reagent bottle at room temperature to be used in the ZnO synthesis.

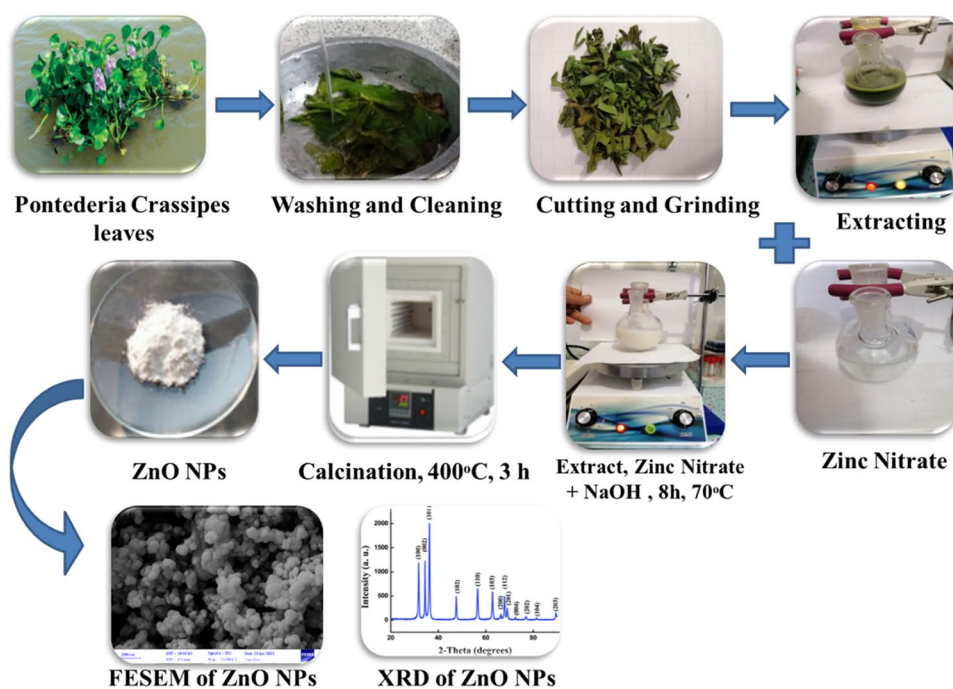
#### 2.1.2 Green synthesis of ZnO NPs

For the synthesis of ZnO NPs, 2.975 g of  $\text{Zn}(\text{NO}_3)_2 \cdot 6\text{H}_2\text{O}$  was gently dissolved into 90 mL distilled water and 10 mL of leaves extract of *Pontederia crassipes* was added. After that, the solution was continuously stirred using a magnetic stirrer for 2 h. This was followed by slow addition of sodium hydroxide (1 M) until the solution pH reached 10 while continuing to stir for an additional 6 h at 70 °C. The obtained white precipitate was separated using centrifugation at 8000 rpm for 30 min. After that, the resultant product was dried in a vacuum oven at 80 °C for 4 h. The final step is calcination of the white powder in a muffle furnace at 400 °C for 3 h. The sample was then kept in an airtight glass container for later usage. The synthesis process is depicted schematically in Fig. 1.

### 2.2 Characterization and instrumentations

FT-IR spectra were obtained from a FT-IR spectrophotometer (A Nicolet 6700 FT-IR) by the KBr disks method

**Fig. 1** Green synthesis of ZnO NPs using *Pontederia crassipes* leaf extract



within the range of 4000–400  $\text{cm}^{-1}$  (Fig. 2). X-ray diffraction analysis of synthesized ZnO NPs was carried out using PANalytical X’Pert Pro diffractometer with Cuk radiation source (0.15405 nm) and a scanning range of 0° to 80°. The morphological properties of the ZnO sample were characterized using ZEISS SIGMA VP scanning electron microscopy. Elemental distribution in the ZnO sample was conducted during FE-SEM analysis using an Oxford EDS device. The size of ZnO NPs was tested using transmittance electron microscopy (ZEISS-EM10C-100 kV). The surface area and porosity of ZnO powder were determined using Quantachrome Instruments (Nova 2200e, USA). A pH meter (211-Instrument Hanna, Romania) was used to adjust the

pH of dye solutions. Ultrasonic dispersion of ZnO NPs was carried out employing an ultrasonic bath (405 power sonic, Hwashin, Korea).

### 2.3 Batch adsorption experiment

For the comparison of adsorption efficiency, contact time (0–120 min), ZnO dose (0.4–2.0 g/L), pH (2–10), initial concentration of dyes (10–75 mg/L), temperature (288–308 K), and ionic strength (0.02–0.07 N) were investigated. In this regard, the batch adsorption process, as described previously, was conducted [26]. Firstly, in a 150-mL conical flask, a certain amount of ZnO NPs was introduced to 100 mL of dye solution. The pH of the solution was adjusted using 0.1 M HCl or 0.1 M NaOH. At 25 °C, the flask was stirred in an orbital shaker at 150 rpm. After the stipulated time period, the adsorbent particles were separated via centrifugation at 8000 rpm for 15 min and absorbance was monitored at  $\lambda_{\text{max}}$  of dye (495 nm for CR and 617 nm for MG). For this, the general approach outlined above was used, with the desired parameter being varied while the others were kept constant. At each interval time, the removal efficiency (%) and adsorption capacity ( $Q_e$ ) were calculated by adopting Eqs. (1) and (2), respectively [27]:

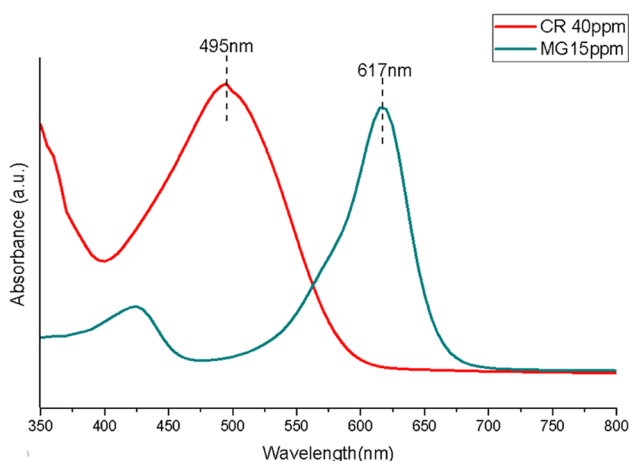


**Fig. 2** UV–Vis spectra of CR and MG dyes

$$\text{Removal \%} = \frac{C_o - C_e}{C_o} * 100 \tag{1}$$

$$Q_e = V(C_o - C_e)/m \tag{2}$$

where:  $C_0$  and  $C_e$  represent the initial concentration (mg/L) and final concentration of dye (mg/L),  $V$  is the volume of dye solution (L), and  $m$  (g) is the amount of ZnO used [28].

## 2.4 Effect of cytotoxicity

MCF7 (a human breast cancer cell line) was purchased from the National Cell Bank of Iran (Pasteur Institute, Iran). Cells were grown in RPMI-1640 medium (Gibco) with 10% FBS (Gibco) supplemented with antibiotics (100 U/mL penicillin and 100  $\mu$ g/mL streptomycin). Cells were maintained at 37 °C under humidified air containing 5% CO<sub>2</sub> and were passaged using trypsin/EDTA (Gibco) and phosphate-buffered saline (PBS) solution. Culturing media and conditions used to grow the cells as 3D colonies were the same as those in monolayer cell culture.

## 3 Results and discussion

### 3.1 Characterization

#### 3.1.1 FT-IR analysis

FT-IR of synthesized ZnO NPs was recorded in the range of 400–4000  $\text{cm}^{-1}$ . FT-IR assists to understand the chemical composition of fabricated ZnO NPs. The FT-IR spectra of ZnO samples are demonstrated in Fig. 3a. The bands of bare ZnO NPs can be at 514  $\text{cm}^{-1}$ , 1095  $\text{cm}^{-1}$ , and 1480  $\text{cm}^{-1}$ . The FT-IR bands of ZnO NPs at 514  $\text{cm}^{-1}$  and 1095  $\text{cm}^{-1}$  correspond to Zn–O bond vibrations, which indicates the successful green synthesis of ZnO NPs. The band centered at 1480  $\text{cm}^{-1}$

relates to the existence of trace phytochemicals adsorbed on the ZnO surface which acted as reducing, capping, and stabilizing agents [29].

#### 3.1.2 Crystallinity and phase

XRD powder technique is employed to provide detailed information about the crystalline phase and crystallite size of ZnO NPs. The XRD pattern of fabricated ZnO NPs is displayed in Fig. 3b. The XRD pattern of ZnO NP powder was obtained from the range of 0°–80°. X-ray diffraction pattern exhibited nine distinguished peaks at  $2\theta$  angles centered at 31.75°, 34.39°, 36.36°, 47.54°, 56.65°, 63.17°, 68.09°, 69.20°, and 77.03° which assigned to crystal planes of (100), (002), (101), (102), (110), (103), (200), (112), (201), and (202), respectively [30]. The fabricated ZnO NPs exhibited sharp diffraction peaks with a single crystalline phase which could be indexed as the hexagonal ZnO wurtzite phase (JCPDS Card no. 36–1451). It also confirms that there no characteristic XRD peak is detected due to any other material or phase indicating the synthesized sample was free of impurities. The crystalline size of ZnO NPs was estimated from the Scherrer equation:

$$D = 0.9\lambda / \beta \cos\theta \quad (3)$$

where  $D$  is the crystalline size (nm),  $\lambda$  is the wavelength of  $\text{CuK}\alpha$  radiation (0.15406 Å),  $\beta$  is the full width at half maximum intensity of the reflection peak, and  $\theta$  is the reflection angle (°). The crystalline size of the ZnO NPs estimated from the XRD pattern is 39 nm.

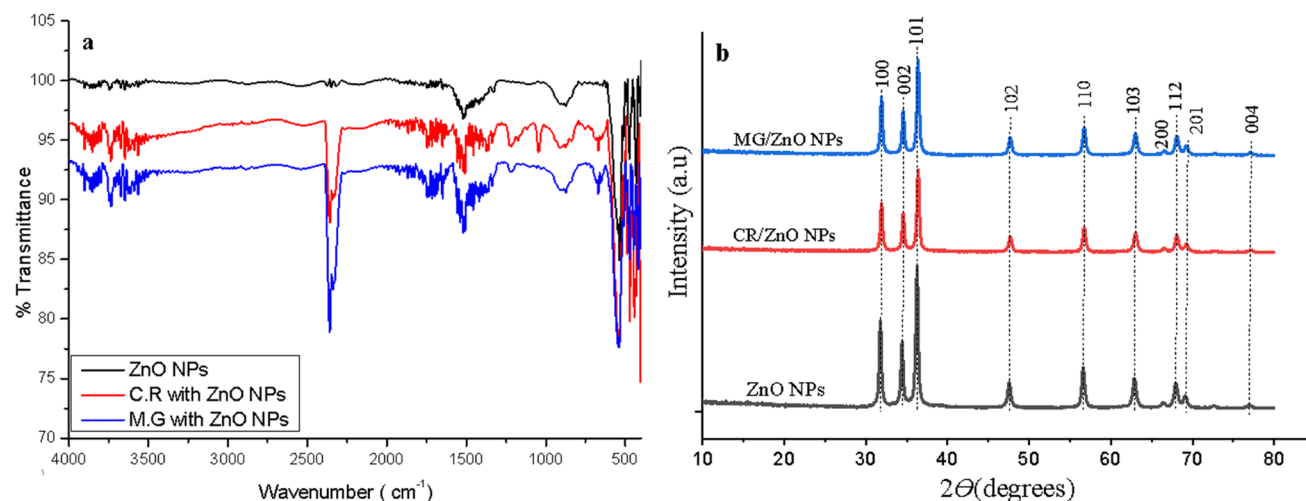


**Fig. 3** FT-IR spectra (a) and XRD patterns (b) of ZnO sample before and after adsorption of CR and MG dyes

### 3.1.3 Surface area and porosity analysis

The specific surface area ( $a_{s,BET}$ ) of synthesized ZnO powder was analyzed using Brunauer–Emmett–Teller (BET) analyzer via  $N_2$  adsorption-desorption isotherms at 77 K. Mean pore diameter was also obtained using the Barrett–Joyner–Halenda (BJH) method. The  $N_2$  adsorption-desorption isotherm and pore size distribution curves of the ZnO sample are demonstrated in Fig. 4a and b. The  $N_2$  adsorption-desorption isotherm of the sample showed a typical IV curve with a hysteresis loop of type H3 confirming the existence of a mesoporous surface. The surface area of the sample determined using the standard multi-point BET method was  $12.794 \text{ m}^2 \text{ g}^{-1}$ . Based on the obtained results, the sample has a 3.331 nm average pore diameter. According to the IUPAC classification, materials that have a pore size diameter in the range of 2–50 nm are classified as microporous.

### 3.1.4 Morphology and elemental distribution analysis

The surface morphology of the synthesized nanomaterials can be examined by employing FE-SEM analysis. Figure 5 shows the FE-SEM images of the ZnO NPs synthesized using *Pontederia crassipes* leaf extract. Figure 5 shows that FE-SEM images were demonstrated in two magnifications: 200 nm and 1  $\mu$ . The morphology of the nanoparticles varies from small spherical particles to big polyhedral nanoparticles. According to the FE-SEM images, most ZnO NPs had a spherical-like morphology with some agglomeration in cluster form. From FE-SEM images, it can be noticed that the particle sizes are clearly of the order of few nanometers. The formation of ZnO

NPs was confirmed by energy dispersive X-ray spectrometry analysis (EDX). Figure 5c displays the results of the (EDX), and it clearly indicates that the weight ratio of Zn and O elements was 89.4% and 10.6%, respectively. The EDX analysis revealed that the required phase of Zn and O is present in the sample and indicated high purity for the fabricated ZnO NPs. The EDX data in the current study exhibit similar Zn and O ratios close to the theoretical values. In general, the EDX technique indicates the presence of metallic zinc oxide in the green synthesized sample.

### 3.1.5 Particle sizes

The mean particle sizes, shape, and distribution of ZnO Nps were evaluated using the TEM technique. Figure 6a displays the TEM micrograph of fabricated ZnO NPs via the green approach using *Pontederia crassipes* leaf extract. The TEM image clearly shows that the ZnO NPs consisted of spherical and hexagonal lamellar-like shapes and mostly with particle sizes smaller than 100 nm. Moreover, the nanoparticles are distributed with a major axis of 20–120 nm and a minor axis of 40–100 nm as can be observed in Fig. 6b. In addition, the TEM images show significant agglomerations of nanoparticles which may be due to annealing of the sample at an almost high temperature. It is reported previously that the surface energy and specific surface area of nanoparticles are significantly higher than those of larger particles; hence, the nanoparticles tend to agglomerate in liquid media at high temperature [31]. The particle size distribution histogram was conducted based on the counted 100 NPs. The mean size of the particles is 64.37 nm.

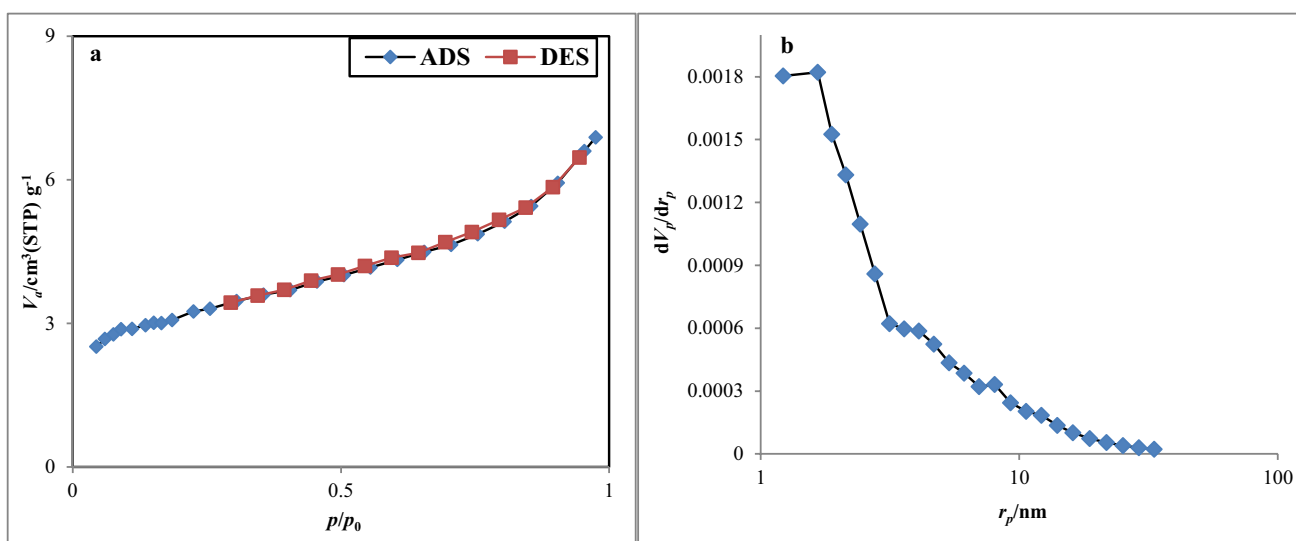


**Fig. 4**  $N_2$  sorption isotherm (a) and pore size distributions (b) of the ZnO NPs

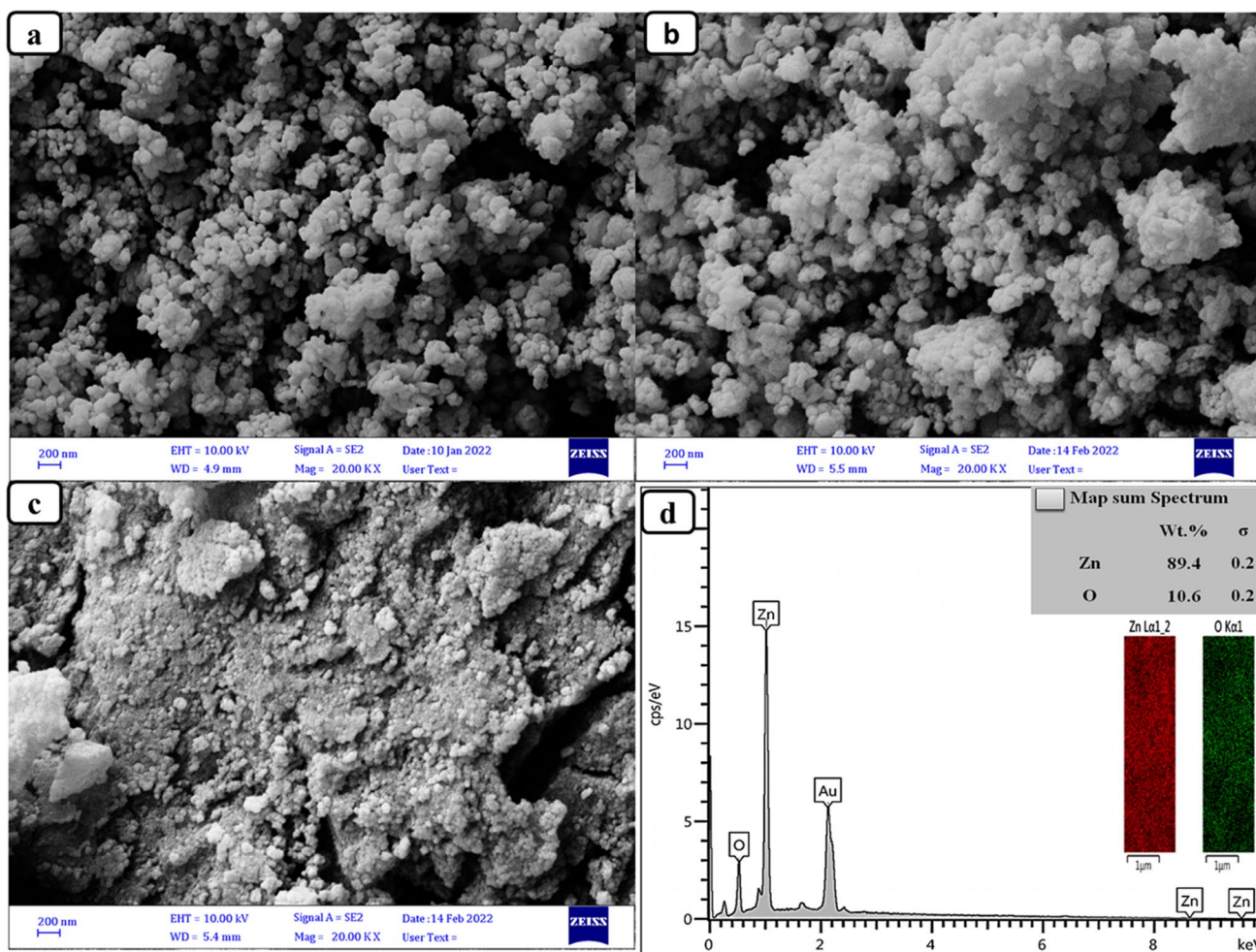


**Fig. 5** FE-SEM images of pure ZnO NPs (a), after adsorption of CR dye (b), after adsorption of MG dye (c), and with EDX analysis and elemental mapping (inset) of pure ZnO NPs (d)

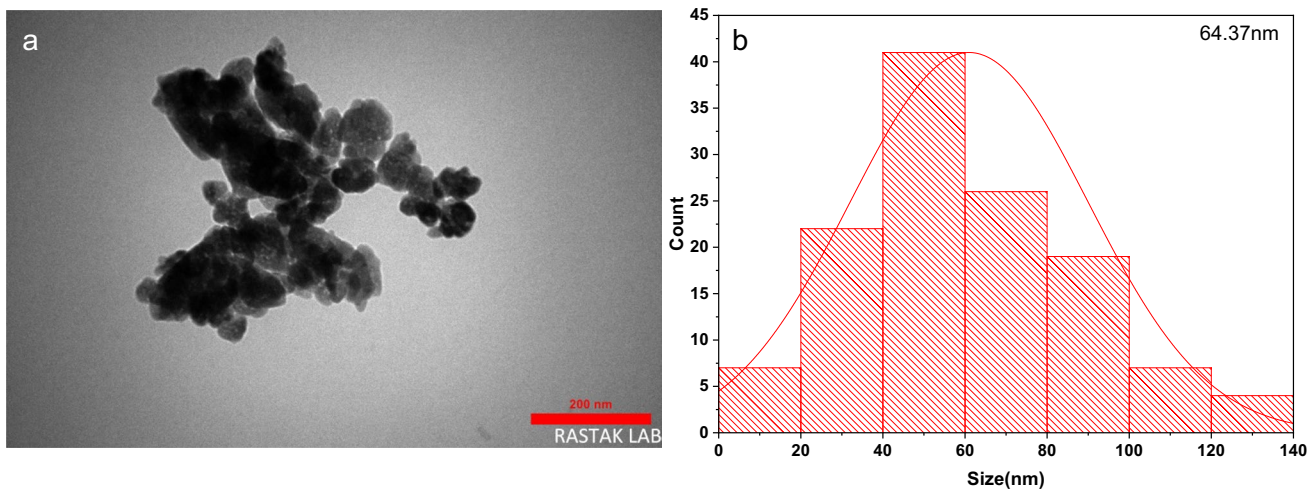


**Fig. 6** TEM image (a) and histogram (b) of ZnO NPs

## 3.2 Adsorption of MG and CR by ZnO NPs

### 3.2.1 Effect of contact time

The influence of contact time on MG and CR removal by ZnO NPs was investigated over a period of 0–120 min in order to determine the equilibrium time of adsorption, using 0.4 g/L of ZnO NPs and 40 and 15 mg/L of CR and MG dyes, respectively. It can be seen from Fig. 7a that the adsorption process is time-dependent and the removal efficiency of both dyes by sorption over ZnO NPs was found to be fast at the initial contact time and then slow down until reaching a constant value where no more dye molecules are removed from the suspension. The results revealed that the equilibrium time of MG and CR sorption onto ZnO NPs was investigated to be 60 and 30 min, respectively. Obviously, at equilibrium time, the adsorption efficiency reached up to 95.68% (CR) and 82.40% (MG). Because no change in adsorption efficiency was detected beyond these periods, the time for further studies was fixed at 60 min for MG and 30 min for CR.

### 3.2.2 Effect of adsorbent dose

Adsorbent dose is an important operational variable because it investigates the adsorption capacity of an adsorbent for a given operating condition. The influence of ZnO adsorbent dosage (0.4–2.0 g/L) was investigated at 298 K and pH 6. As can be seen in Fig. 7b, the ZnO adsorbent exhibited the maximum removal efficiency at 1.2 g/L for both dyes. For CR dye, the adsorption efficiency increased from 94.82% to 96.03% for an adsorbent dose increase from 0.4 to 1.2 g/L, respectively. For MG dye, in the same adsorbent dose range,

the removal efficiency increased from 80.70 to 85%. At low adsorbent doses, the removal efficiency increases with an increase in adsorbent dose which is due to the increase in the availability of a number of active sites owing to the increase in the total surface area. It was obvious from Fig. 6 that the constancy in removal efficiency with increasing adsorbent dose beyond 1.2 g/L could be attributed to partial blocking of active sites as a result of particle agglomerations. Therefore, the adsorbent dose was fixed at 1.2 g/L for both dyes because adsorption was undetectable above this value [32]. Similar behavior was reported by other research groups and it was proposed that an increase in adsorbent dosage, in addition to decreasing of effective surface area the diffusion path length increases, causes dropping in removal efficiency [33, 34].

### 3.3 Effect of pH

The solution pH plays a major role in the adsorption of water contaminations onto adsorbents, which charges of adsorbent surface. The pH impact was studied in the ranges of 2–10 and 2–8 for CR and MG, respectively, while the other parameters were kept constant. Figure 8 shows the effect of solution pH on the adsorption efficiency of CR and MG dyes onto ZnO NPs. The maximum CR adsorption efficiency was obtained to be 96.39% at pH 2.0, while the maximum adsorption efficiency of MG dye was 97.10 at pH 8. For CR dye, by increasing the pH, the adsorption efficiency was decreased. At pH 2, the surface ZnO NPs turn positively charged and adsorption is enhanced due to the electrostatic attraction of negatively charged CR molecules with the surface. The decline in adsorption capacity in alkaline solution is due to competition between anionic CR molecules

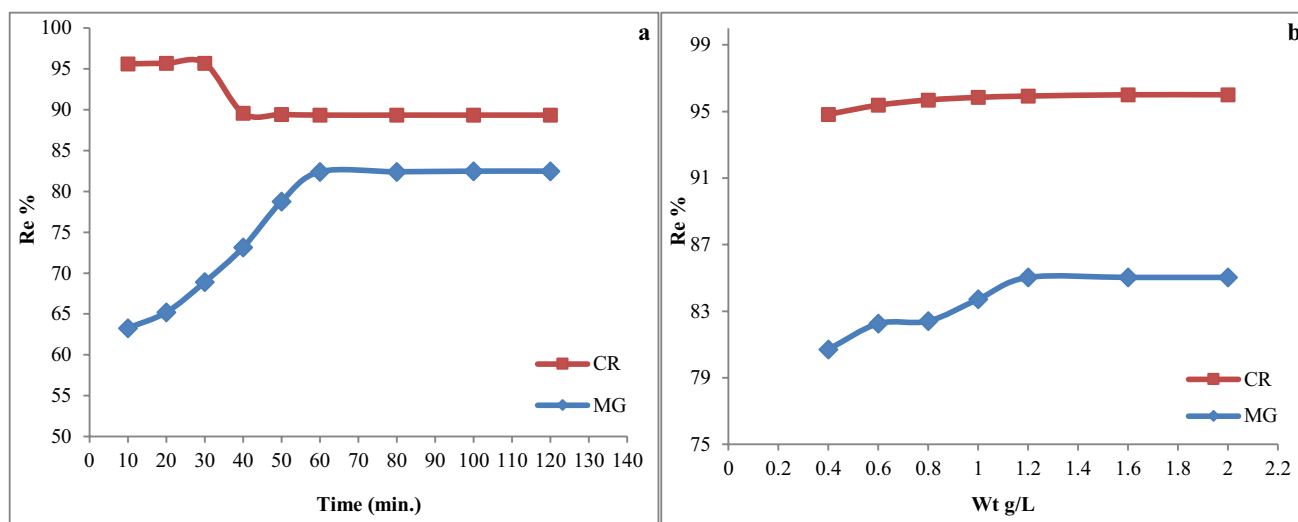


**Fig. 7** Effect of contact time (a) and adsorbent dose (b) on MG and CR adsorptive removal onto ZnO NPs at 298 K

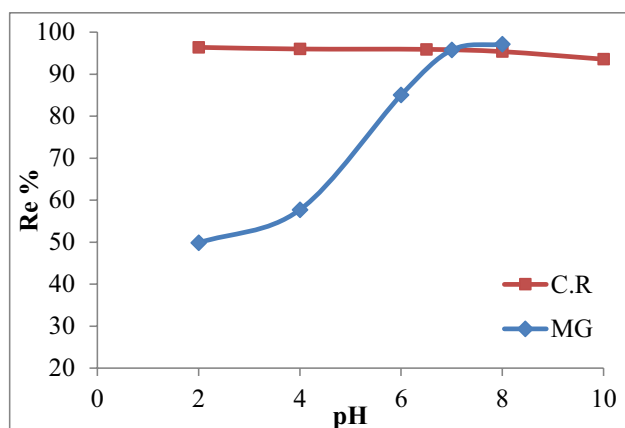


**Fig. 8** Effect of pH on the CR and MG dyes adsorption over ZnO NPs ( $[CR] =$ ,  $[MG] =$ ; adsorbent dose =; temperature, 298 K

and hydroxyl anions. Regarding the positively charged MG dye, the behavior is reversed. Figure 7 clearly exhibits that alkaline solution favored the adsorption of MG dye and the maximum adsorption efficiency was reached at a pH value of 8. The low adsorption efficiency of MG over ZnO NPs at pH<sub>s</sub> 2–6 could be due to the availability of excess H<sup>+</sup> cations that compete with the positive dye molecules for the adsorption sites. At pH beyond 7, the adsorption efficiency drops probably due to the formation of soluble hydroxyl complexes [35]. These results demonstrated that the solution pH had a variable impact on the adsorption of dyes depending on the nature of the dye charge.

### 3.4 Effect of ionic strength

Another important factor affecting the concentration of water contaminations is ionic strength which might influence the adsorption efficiency of dyes. Ionic strength effect on the adsorptive removal of CR and MG dyes was investigated

using various electrolytes (NaCl, KCl, CaCl<sub>2</sub>, and AlCl<sub>3</sub>) at various concentrations ranging from 0.02 to 0.07 N. As shown in Fig. 9a and b, for both dyes, the adsorption efficiency decreased with the increase in electrolyte concentration, but the electrolytes had a greater effect in reducing MG adsorption than CR. In addition, the results showed a retard in the adsorption efficiency depends on the charge and size of ions. As can be observed, the ions with the largest charge (Mg<sup>+2</sup> and Ca<sup>+2</sup>) reduced the adsorption efficiency more than the ions with the lowest charges (Na<sup>+1</sup> and K<sup>+1</sup>). Generally, the possible reason behind the dropping of adsorption efficiency at high electrolytes is due to the screening of electrostatic interaction of opposite charges by the electrolyte on the ZnO NPs surface. As shown in the results, the adsorption efficiency of CR was not significantly affected, whether when varying the concentration and salt type. On the other hand, the decline in MG removal efficiency is significant in the case of changing the salt concentration and ion charge. The efficiency of MG adsorption decreased from its maximum value (97.10%) to the lowest one (69.01%) when using CaCl<sub>2</sub> (0.07 N).

### 3.5 Effect of temperature

The temperature is regarded as the most important parameter in the adsorption process for any materials on a solid surface. Investigating the effect of temperature on the adsorption process will help explain the mechanism by which adsorption occurs, whether it is physisorption or chemisorption. The thermodynamic study was performed at a temperature range of 288–315 K while the other variables were kept constant (contact time, adsorbent dosage, initial dye concentration, and initial pH). The thermodynamic parameters, Gibb's free energy change ( $\Delta G^\circ$ ), enthalpy change ( $\Delta H^\circ$ ), and entropy change ( $\Delta S^\circ$ ), were determined by Eqs. (4) to (7) [36]. Figure 10a and b show the effect of temperature on the adsorption capacity and

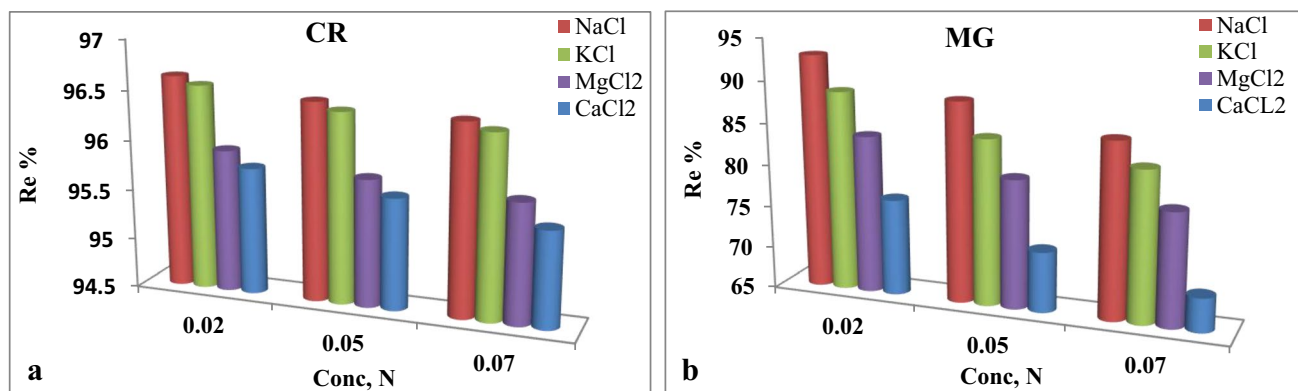


**Fig. 9** Effect of ionic strength on adsorption of CR (a) and MG (b) onto ZnO NPs



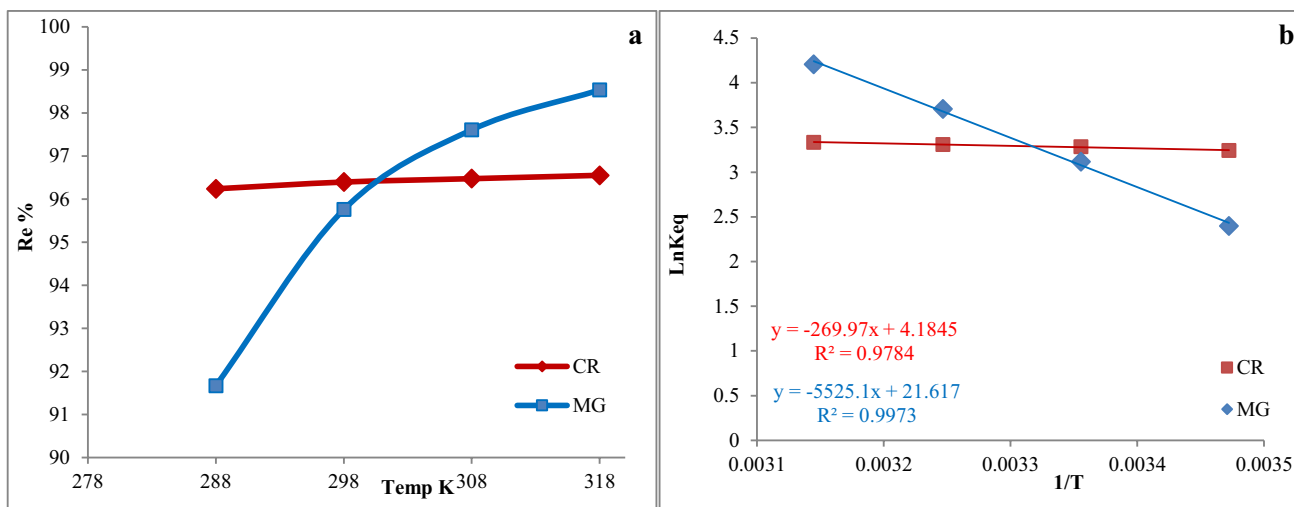


**Fig. 10** Effect of temperature on adsorption of CR and MG on ZnO NPs (a) and Plots of Van't Hoff's equation (b)

adsorption efficiency, respectively. Figure 9c illustrates the Van't Hoff plot of the effect of temperature on the adsorption behavior of CR and MG onto ZnO NPs. The values of thermodynamic parameters are represented as follows:

$$K_{eq} = \frac{Q_E \times m}{C_e \times V} \tag{4}$$

$$\Delta G^\circ = -RT \ln K_{eq} \tag{5}$$

$$\ln K_{eq} = \frac{-\Delta H^\circ}{RT} + \text{con.} \tag{6}$$

$$\Delta S^\circ = \frac{\Delta H^\circ - \Delta G^\circ}{T} \tag{7}$$

where  $K_{eq}$  refers to the equilibrium adsorption constant,  $T$  is the absolute temperature (K), and  $R$  is the ideal gas constant ( $R = 8.3144 \text{ J mol}^{-1} \text{ K}^{-1}$ ). Obviously, the results in Fig. 9 and Table 1 suggest that the adsorption processes for both dyes are endothermic and spontaneous. In the case of both dyes, the adsorption efficiency begins to increase as the temperature increases which means the exothermic nature of the adsorption cycle. According to Fig. 9a, an increase in the adsorption efficiency from 91.66 to 98.33% for MG was noticed as the temperature was raised from 288 to 318 K. As for the adsorption of CR dye, it was slightly influenced, where the adsorption efficiency increased from 96.22 to 96.55% within the same previous thermal range. This behavior can be supported by a low enthalpy value (2.244 kJ/mol) as can be observed in Fig. 9b and Table 1.

In addition, the positive values of  $\Delta S^\circ$  indicate a high rate of randomness of adsorbed species at the

**Table 1** Thermodynamic parameters of the adsorption of the CR and MG over ZnO NPs

Adsorbate	Temp. K	$-\Delta G^\circ$ (kJ/mol)	$\Delta H^\circ$ (kJ/mol)	$\Delta S^\circ$ (J/mol K)
CR	288	7.76261	2.244531	34.74701
	298	8.14162		34.85285
	308	8.47319		34.79779
	318	8.80986		34.76222
MG	288	5.7416	45.93568	179.4351
	298	7.72096		180.0558
	308	9.49727		179.9771
	318	11.1249		179.4357

adsorbent–adsorbate interfaces of both CR and MG dyes. Finally, the values of  $\Delta H^\circ$  indicate that the adsorption type for both dyes is physisorption [37–39].

### 3.6 Adsorption isotherms

Adsorption isotherms are basic requirements for the correlation of the residual concentration of CR and MG dyes in the aqueous solution and adsorption capacity to design the adsorption systems. To complement the adsorption process, the experimental results of the effect of temperature on the adsorption process were adjusted using the Langmuir, Freundlich, and Temkin isotherm models. The results are shown in Figs. 11 and 12 and Table 2.

#### 3.6.1 Langmuir isotherm

This Langmuir equation describes the adsorption with monolayer where the thickness of the adsorbed layer is equal to

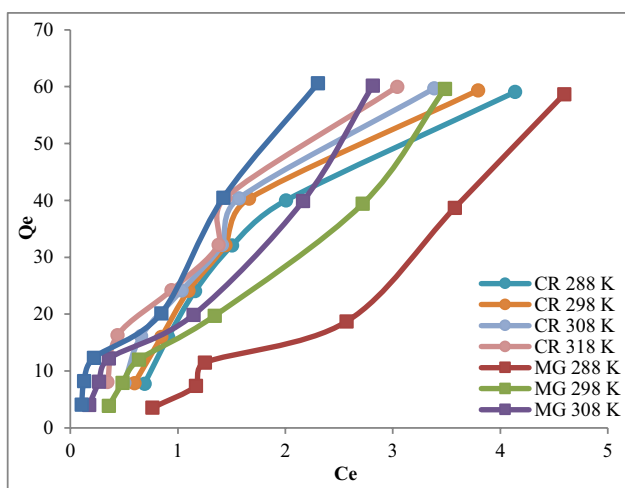


**Fig. 11** Adsorption isotherms of CR and MG dyes

one molecule. The linear formula of Langmuir’s equation was adopted to investigate the adsorption process for the CR and MG dye as follows [40]:

$$\frac{C_e}{Q_e} = \frac{1}{ab} + \frac{C_e}{a} \tag{8}$$

where  $a$  is a maximum adsorption capacity (mg/g) corresponding to monolayer coverage and  $b$  is the Langmuir constant (mg/L). The linear plot of Langmuir isotherm of CR and MG dyes is shown in Fig. 12a and b. The essential feature of the Langmuir isotherm is represented as a dimensionless separation factor  $R_L$  [41].

$$R_L = \frac{1}{(1 + bC_0)} \tag{9}$$

where  $R_L$  values indicate the favorability of the Langmuir isotherm model: favorable ( $0 < R_L < 1$ ), unfavorable ( $R_L > 1$ ), linear ( $R_L = 1$ ), and irreversible ( $R_L = 0$ ).

**Fig. 12** The plot of linear formula of isotherms for CR and MG adsorption onto ZnO NPs: Langmuir (a, b), Freundlich (c, d), and Temkin (e, f)

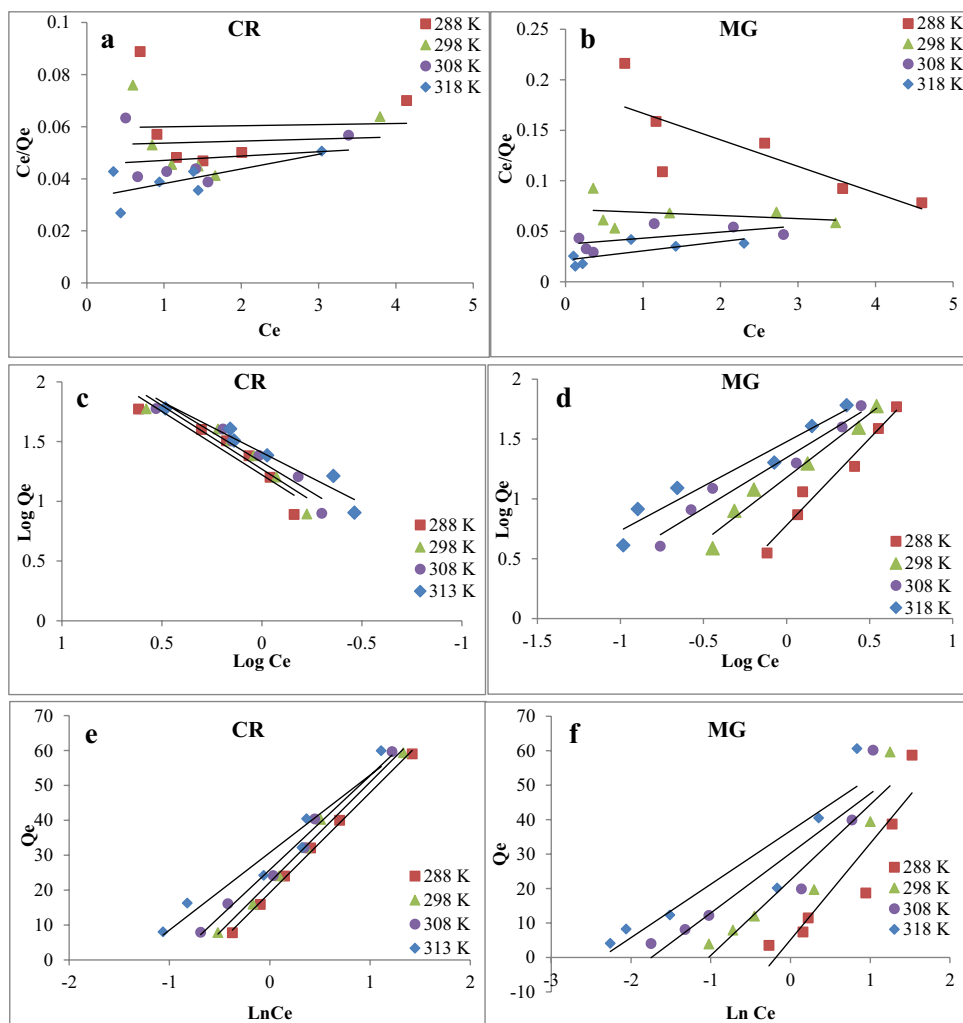


**Table 2** Parameters of adsorption isotherms

	Temp K	Langmuir isotherm				Freundlich isotherm			Temkin isotherm		
		a (mg/g)	b (mg/L)	( $R^2$ )	$R_L$	( $K_f$ )	( $n$ )	( $R^2$ )	$B_T$	$A_T$	( $R^2$ )
CR	288	2500	0.0067	0.0011	0.7886	16.683	0.9415	0.8806	28.731	1.9535	0.9976
	298	1250	0.0151	0.0074	0.6234	18.599	0.9384	0.8957	28.679	2.1703	0.9900
	308	588.23	0.0374	0.0315	0.4003	21.252	0.9872	0.9245	26.971	2.606	0.9853
	318	178.57	0.1723	0.4733	0.1267	25.603	1.1768	0.9376	22.185	3.999	0.9429
MG	288	-38.022	-0.1361	0.6316	-0.9597	6.0089	0.6889	0.9665	27.977	1.1999	0.8573
	298	-322.58	-0.0431	0.0844	2.8372	15.079	0.9370	0.968	21.888	2.7935	0.9046
	308	166.66	0.1621	0.3524	0.2913	22.146	1.1801	0.9592	17.304	5.7472	0.8574
	318	108.69	0.4319	0.5443	0.1337	30.012	1.3464	0.9419	15.48	10.729	0.8602

### 3.6.2 Freundlich isotherm

This Freundlich equation suggests multilayer adsorption. The adsorption sites have a non-uniform affinity for the adsorbate molecules and interactions between sorbed molecules present. The Freundlich model is given by the following expression [42]:

$$\text{Log}Q_e = \text{Log}K_f + \frac{1}{n}\text{Log}C_e \quad (10)$$

where  $K_f$  (L/mg) is the Freundlich isotherm constant and  $n$  is the adsorption parameter related to the adsorption intensity. The linear plot of the Freundlich equation of CR and MG dyes is shown in Fig. 12c and d.

### 3.6.3 Temkin isotherm

Temkin isotherm model describes the interaction between adsorbent and adsorbate and heat generated due to the adsorption process. The Temkin isotherm is given as follows [43]:

$$Q_e = B\ln A_T + B\ln C_e \quad (11)$$

where  $A_T$  represents the equilibrium binding energy and constant  $B$  represents the adsorption heat. The linear plot of the Temkin equation of CR and MG dyes is shown in Fig. 12e and f.

As ( $R^2$ ) exhibited in Table 2, the Temkin isotherm seems to be more applicable than Langmuir and Freundlich isotherms for the description of adsorption of CR dye. This indicates that the adsorption enthalpy of dye molecules in the sorption layer declined linearly with the increase in ZnO surface coverage [44]. On the other hand, the Freundlich model is more applicable to Langmuir and Temkin isotherm for the adsorption of MG dye which indicates that the adsorption is heterogeneous and multilayered [45]. These results showed that the uniform distribution of functional

groups both on the dye and adsorbent surfaces resulted in a uniform distribution of binding energies.

## 4 Kinetic study

The adsorption kinetics is an important factor in order to examine the design of the adsorption process and to investigate the ZnO behavior for Cr and MG dyes remediation as water pollutants. To study the adsorption kinetics, the experimental data was subjected to the pseudo-first-order and pseudo-second-order kinetic models. A linear form of the pseudo-first-order model was described by Lagergren in the following expression [46]:

$$\text{Long}(q_e - q_t) = \text{long } q_e - \frac{K_1 t}{2.303} \quad (12)$$

where  $q_e$  (mg/g) is the adsorption capacity and  $k_1$  is the first-order constant ( $\text{min}^{-1}$ ). In the pseudo-second-order model, Eq. (4) was applied to investigate the adsorption kinetics of CR and MG on ZnO NPs and has the general form as [47]:

$$\frac{t}{q_t} = \frac{1}{K_2 q_e^2} + \frac{t}{q_e} \quad (13)$$

where  $K_2$  is the second-order constant (g/mg min). According to the results shown in Fig. 13a and b and Table 3, it can be indicated that the pseudo-second-order kinetic model best fit the experimental equilibrium data for the description of the adsorption of CR and MG dye onto ZnO NPs.

## 5 Evaluation of ZnO NP cytotoxicity in MCF7 cells

Cell growth and cell viability were quantified using the MTT [3-(4, 5-dimethylthiazol-2-yl)-2, 5-diphenyltetrazolium Bromide] (Sigma-Aldrich) assay. In brief, for monolayer culture, cells (MCF7) were digested with trypsin, harvested,

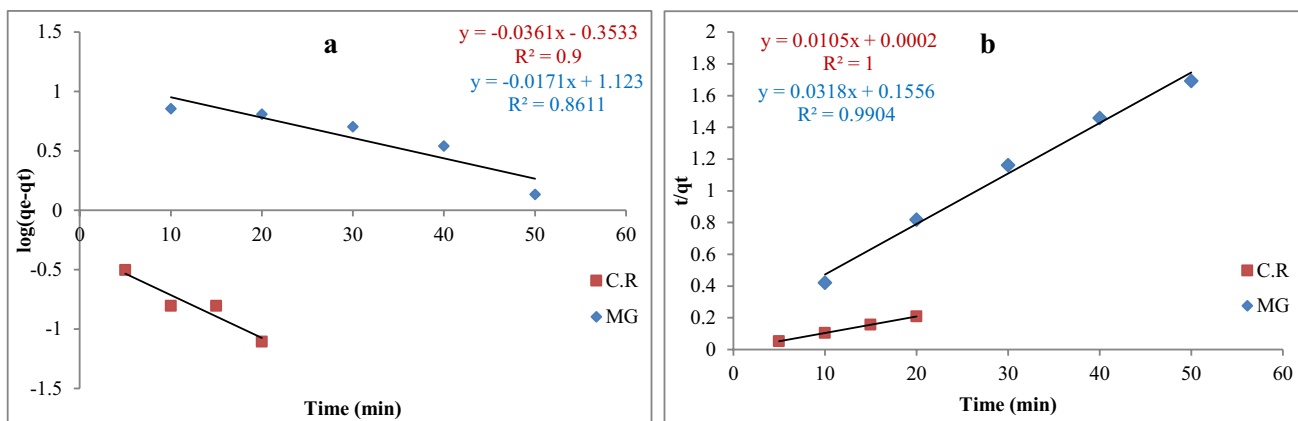


Fig. 13 Adsorption kinetics of CR and MG on ZnO NPs pseudo-first-order model (a) and pseudo-second-order model (b)

Table 3 Kinetic parameters of CR and MG adsorption onto ZnO NPs

Pseudo – first – order	$K_1$	$q_e$	$r^2$
MG	0.0393	13.2739	0.8611
CR	0.0831	0.4433	0.9
Pseudo – second – order	$K_2$	$q_e$	$r^2$
MG	0.0064	31.4465	0.9904
CR	0.5512	95.238	1

adjusted to a density of  $1.4 \times 10^4$  cells/well, and seeded to 96-well plates filled with 200  $\mu$ l fresh medium per well for 24 h. When cells formed a monolayer, they were treated with 12.5–200  $\mu$ g/ml of the compounds for 24 h at 37 °C in 5% CO<sub>2</sub>. At the end of the treatment (24 h), while the monolayer culture was left untouched in the original plate, the supernatant was removed and 200  $\mu$ l/well of MTT solution (0.5 mg/mL in phosphate-buffered saline [PBS]) was added and the plate was incubated at 37 °C for an additional 4 h. MTT solution (the supernatant of cells was removed and DMSO was added (100  $\mu$ l per well). Cells were incubated on a shaker at 37 °C until crystals were completely dissolved. Cell viability was quantified by measuring absorbance at 570 nm using an ELISA reader (Model wave xs2, BioTek, USA). The concentration of the compounds that resulted in 50% of cell death (IC<sub>50</sub>) was determined from respective dose–response curves as shown in Table 4 and Fig. 14 [48].

### 6 Conclusions

The current study demonstrated the synthesis of ZnO NPs with a safe, facile, and effective route using an aqueous leaf extract of *Pontederia crassipes*. The characterization results showed the successful synthesis of a nearly uniform hexagonal wurtzite structure of ZnO NPs with an average particle size of 64.37 nm. The green synthesized ZnO NPs exhibited excellent adsorption for CR and MG dyes that followed Temkin and Freundlich isotherm models, respectively. The adsorption of both dyes is endothermic and spontaneous and matches the pseudo-second-order kinetics. Moreover, the green synthesized ZnO NPs exhibited inhibitory effects on

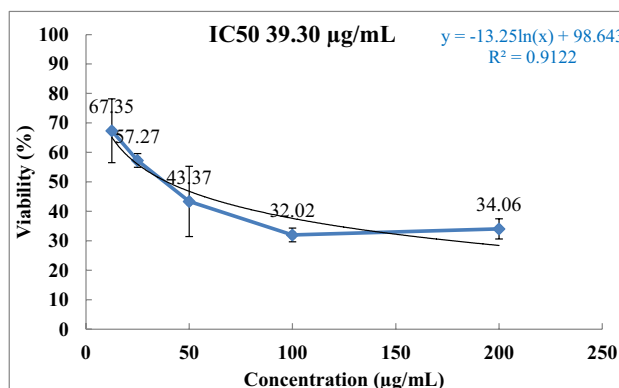


Fig. 14 MTT cell viability assay in MCF7 cells on ZnO NPs

Table 4 MTT cell viability assay in MCF7 cells on ZnO NPs

Sample ID	ZnO NPs									
	Concentration ( $\mu$ g/mL)									
	12.5	25	50	100	200					
Absorption at 570 nm	0.234	0.294	0.231	0.218	0.137	0.203	0.132	0.119	0.124	0.143
Viability (%)	59.69	75.00	58.93	55.61	34.95	51.79	33.67	30.36	31.63	36.48
Average viability (%)	67.35	57.27	43.37	32.02	34.06					
Standard deviation ( $\pm$ )	10.82	2.34	11.91	2.34	3.43					

the MCF7 cancer cell line. In general, the results confirmed that ZnO NPs can be fabricated by adopting *Pontederia cras-sipes* as a renewable agent (eco-friendly route) excluding the use of any harmful chemicals. Finally, the results revealed that the green fabricated ZnO NPs could be employed as a promising anti-cancer agent.

## Declarations

**Conflict of interest** The authors declare no competing interests.

## References

- Kumar A, Sharma SK, Sharma G, Naushad M, Stadler FJ (2020) CeO<sub>2</sub>/g-C<sub>3</sub>N<sub>4</sub>/V<sub>2</sub>O<sub>5</sub> ternary nano hetero-structures decorated with CQDs for enhanced photo-reduction capabilities under different light sources: dual Z-scheme mechanism. *J Alloy Compd* 838:155692
- Mashkoo F, Nasar A (2020) Magsorbents: potential candidates in wastewater treatment technology-a review on the removal of methylene blue dye. *J Magn Magn Mater* 500:166408
- Sartape AS, Mandhare AM, Jadhav VV, Raut PD, Anuse MA, Kolekar SS (2017) Removal of malachite green dye from aqueous solution with adsorption technique using *Limonia acidissima* (wood apple) shell as low cost adsorbent. *Arab J Chem* 10:S3229–S3238
- Zhou G, Cao Y, Jin Y, Wang C, Wang Y, Hua C, Wu S (2020) Novel selective adsorption and photodegradation of BPA by molecularly imprinted sulfur doped nano-titanium dioxide. *J Clean Prod* 274:122929
- Alver E, Bulut M, Metin AÜ, Çiftçi H (2017) One step effective removal of congo red in chitosan nanoparticles by encapsulation. *Spectrochim Acta Part A Mol Biomol Spectrosc* 171:132–138
- Tu NTT, Thien TV, Du PD, Chau VTT, Mau TX, Khieu DQ (2018) Adsorptive removal of congo red from aqueous solution using zeolitic imidazolate framework-67. *J Environ Chem Eng* 6(2):2269–2280
- Abdel-Ghani NT, El-Chaghaby GA, Rawash ESA, Lima EC (2017) Adsorption of coomassie brilliant blue r-250 dye onto novel activated carbon prepared from *nigella sativa* l. waste: equilibrium, kinetics and thermodynamics running title: adsorption of brilliant blue dye onto *nigella sativa* l. waste activated carbon. *J Chilean Chem Soc* 62(2):3505–3511
- Yousif QA, Mahdi KM, Alshamsi HA (2021) Enhanced photo-voltaic performance of dye-sensitized solar cell based on ZnO nanoparticles and ZnO/graphene nanocomposites. *J Chin Chem Soc* 68(9):1637–1643
- Bejar L, Medina A, Herrera G, Vargas R, Bernal L, Alfonso I (2012) Effect of the chemical precipitation synthesis parameters on the morphology and size of ZnO nanoparticles. *Microsc Microanal* 18(S2):1946–1947
- Alshamsi HAH, Hussein BS (2018) Hydrothermal preparation of silver doping zinc oxide nanoparticles: study, characterization and photocatalytic activity. *Orient J Chem* 34(4):898–1907
- Hamidi A, Taghavizadeh Yazdi ME, Amiri MS, Hosseini HA, Darroudi M (2019) Biological synthesis of silver nanoparticles in *Tribulus terrestris* L. extract and evaluation of their photocatalyst, antibacterial, and cytotoxicity effects. *Res Chem Intermed* 45(5):2915–2925
- Taghavizadeh Yazdi ME, Khara J, Sadeghnia HR, Esmaeilzadeh Bahabadi S, Darroudi M (2018) Biosynthesis, characterization, and antibacterial activity of silver nanoparticles using *Rheum turkestanicum* shoots extract. *Res Chem Intermed* 44(2):1325–1334
- Taghavizadeh Yazdi ME, Hamidi A, Amiri MS, Kazemi Oskuee R, Hosseini HA, Hashemzadeh A, Darroudi M (2019) Eco-friendly and plant-based synthesis of silver nanoparticles using *Allium giganteum* and investigation of its bactericidal, cytotoxicity, and photocatalytic effects. *Mater Technol* 34(8):490–497
- Yazdi MET, Khara J, Housaindokht MR, Sadeghnia HR, Bahabadi SE, Amiri MS, ... and Darroudi M (2019) Role of *Ribes khorrassanicum* in the biosynthesis of AgNPs and their antibacterial properties. *IET Nanobiotechnol* 13(2):189–192
- Zarei M, Karimi E, Oskoueian E, Es-Haghi A, Yazdi MET (2021) Comparative study on the biological effects of sodium citrate-based and apigenin-based synthesized silver nanoparticles. *Nutr Cancer* 73(8):1511–1519
- Zabihi E, Babaei A, Shahrampour D, Arab-Bafrani Z, Mirshahidi KS, Majidi HJ (2019) Facile and rapid in-situ synthesis of chitosan-ZnO nano-hybrids applicable in medical purposes; a novel combination of biomineralization, ultrasound, and bio-safe morphology-conducting agent. *Int J Biol Macromol* 131:107–116
- Alavi-Tabari SA, Khalilzadeh MA, Karimi-Maleh H (2018) Simultaneous determination of doxorubicin and dasatinib as two breast anticancer drugs uses an amplified sensor with ionic liquid and ZnO nanoparticle. *J Electroanal Chem* 811:84–88
- Mohamadian F, Eftekhari L, Haghghi Bardineh Y (2018) Applying GMDH artificial neural network to predict dynamic viscosity of an antimicrobial nanofluid. *Nanomedicine J* 5(4):217–221
- Heer ASK (2017) Spectral characterization and anti-fungal activity of zinc oxide (zno) nanoparticles synthesized using *Cynodon dactylon* leaf extract. *World J Pharm Res* 6:16
- Es-haghi A, Javadi F, Yazdi MET, Amiri MS (2019) The expression of antioxidant genes and cytotoxicity of biosynthesized cerium oxide nanoparticles against hepatic carcinoma cell line. *Avicenna J Med Biochem* 7(1):16–20
- Javadi F, Yazdi MET, Baghani M, Es-haghi A (2019) Biosynthesis, characterization of cerium oxide nanoparticles using *Cerato-nia siliqua* and evaluation of antioxidant and cytotoxicity activities. *Mater Res Express* 6(6):065408
- Zhu L, Zeng W (2017) Room-temperature gas sensing of ZnO-based gas sensor: a review. *Sens Actuators A:Phys* 267:242–261
- Ani II, Akpan UG, Olutoye MA, Hameed BH (2018) Photocatalytic degradation of pollutants in petroleum refinery wastewater by TiO<sub>2</sub>-and ZnO-based photocatalysts: recent development. *J Clean Prod* 205:930–954
- Jiang J, Pi J, and Cai J (2018) The advancing of zinc oxide nanoparticles for biomedical applications. *Bioinorg Chem Appl* 2018:1062562
- Malik A (2007) Environmental challenge vis a vis opportunity: the case of water hyacinth. *Environ Int* 33(1):122–138
- Metcalf L, Eddy HP, Tchobanoglous G (1991) *Wastewater engineering: treatment, disposal, and reuse*, vol 4. McGraw-Hill, New York
- Ahmad MA, Rahman NK (2011) Equilibrium, kinetics and thermodynamic of Remazol Brilliant Orange 3R dye adsorption on coffee husk-based activated carbon. *Chem Eng J* 170(1):154–161
- Pelosi BT, Lima LKS, Vieira MGA (2014) Removal of the synthetic dye Remazol Brilliant Blue R from textile industry wastewaters by biosorption on the macrophyte *Salvinia natans*. *Braz J Chem Eng* 31(4):1035–1045
- Vaishnav J, Subha V, Kirubandan S, Arulmohi M, Renganathan S (2017) Green synthesis of zinc oxide nanoparticles by *Celosia*

- Argentina and its characterization. *J Optoelectron Biomed Mater* 9(1):59–71
30. Mahalakshmi S, Hema N, vijaya PP (2020) In vitro biocompatibility and antimicrobial activities of zinc oxide nanoparticles (ZNO NPs) prepared by chemical route—a comparative study. *Bio nano sci* 10:112–121
  31. Moghaddam AB, Moniri M, Azizi S, Rahim RA, Ariff AB, Saad WZ, Namvar F, Navaderi M, Mohamad R (2017) Biosynthesis of ZnO nanoparticles by a new *Pichia kudriavzevii* yeast strain and evaluation of their antimicrobial and antioxidant activities. *Molecules* 22(6):872
  32. Al-Hamdan AZ, Reddy KR (2005) Surface speciation modeling of heavy metals in kaolin: implications for electrokinetic soil remediation processes. *Adsorption* 11(5):529–546
  33. Kibrahim H, Muneer AA, TKreem, E. (2018) Effective adsorption of azure B dye from aqueous solution using snail shell powder. *J Biochem Technol* 9(3):39–44
  34. Xu L, Zheng X, Cui H, Zhu Z, Liang J, and Zhou J (2017) Equilibrium, kinetic, and thermodynamic studies on the adsorption of cadmium from aqueous solution by modified biomass ash. *Bioinorg Chem Appl.* 2017:3695604
  35. Emeniru DC, Onukwuli OD, DouyeWodu PE, Okoro BI (2015) The equilibrium and thermodynamics of methylene blue uptake onto ekowe clay; influence of acid activation and calcination. *Int J Eng Appl Sci* 2(5):257933
  36. Al-Rufaie MM, Alsultani ZTA, Waheed AS (2016) Adsorption kinetics and thermodynamics of azure C dye from aqueous solution onto activated charcoal. *Koroze a Ochrana Materiálu* 60(3):80
  37. Arumugam TK, Krishnamoorthy P, Rajagopalan NR, Nanthini S, Vasudevan D (2019) Removal of malachite green from aqueous solutions using a modified chitosan composite. *Int J Biol Macromol* 128:655–664
  38. Muinde VM, Onyari JM, Wamalwa B, Wabomba J, Nthumbi RM (2017) Adsorption of malachite green from aqueous solutions onto rice husks: kinetic and equilibrium studies. *J Environ Prot* 8:215–230
  39. Hussain N, Alwan S, Alshamsi H, Sahib I (2020) Green synthesis of S- and N-codoped carbon nanospheres and application as adsorbent of Pb (II) from aqueous solution. *Int J Chem Eng* 2020(9068358):1–13
  40. Langmuir I (1918) The adsorption of gases on plane surfaces of glass, mica and platinum. *J Am Chem Soc* 40(9):1361–1403
  41. Deb A, Debnath A, Bhattacharjee N, and Saha B (2020) Ultrasonically enhanced dye removal using conducting polymer functionalised ZnO nanocomposite at near neutral pH: kinetic study, isotherm modelling and adsorbent cost analysis. *Inte J Environ Anal Chem.* <https://doi.org/10.1080/03067319.2020.1843649>
  42. Freundlich H (1907) Über die adsorption in lösungen. *Z Phys Chem* 57(1):385–470
  43. Temkin MJ, and Pyzhev V (1940) Recent modifications to Langmuir isotherms. *Acta Physiochim URSS* 12:217–225
  44. Noreen S, Ismail S, Ibrahim SM, Kusuma HS, Nazir A, Yaseen M, Khan MI, Iqbal M (2021) ZnO, CuO and Fe<sub>2</sub>O<sub>3</sub> green synthesis for the adsorptive removal of direct golden yellow dye adsorption: kinetics, equilibrium and thermodynamics studies. *Z Phys Chem* 35(8):1055–1075
  45. Tewari K, Singhal G, Arya RK (2018) Adsorption removal of malachite green dye from aqueous solution. *Rev Chem Eng* 34(3):427–453
  46. Lagergren S (1898) Zur theorie der sogenannten adsorption geloster stoffe kungliga svenska vetenskapsakademiens. *Handlingar* 24:1–39
  47. Aminu I, Gumel SM, Ahmad WA, Idris AA (2020) Adsorption isotherms and kinetic studies of congo-red removal from waste water using activated carbon prepared from jujube seed. *Am J Anal Chem* 11(47-59):44
  48. Shamasi Z, Es-haghi A, Taghavizadeh Yazdi ME, Amiri MS, Homayouni-Tabrizi M (2021) Role of *Rubia tinctorum* in the synthesis of zinc oxide nanoparticles and apoptosis induction in breast cancer cell line. *Nanomed J* 8(1):65–72

**Publisher's note** Springer Nature remains neutral with regard to jurisdictional claims in published maps and institutional affiliations.